



2nd Advanced Optical Metrology Compendium

Advanced Optical Metrology

Geoscience | Corrosion | Particles | Additive Manufacturing: Metallurgy, Cut Analysis & Porosity



EVIDENT
OLYMPUS

WILEY

The latest eBook from **Advanced Optical Metrology**.
Download for free.

This compendium includes a collection of optical metrology papers, a repository of teaching materials, and instructions on how to publish scientific achievements.

With the aim of improving communication between fundamental research and industrial applications in the field of optical metrology we have collected and organized existing information and made it more accessible and useful for researchers and practitioners.

EVIDENT
OLYMPUS

WILEY

Room-Temperature Micropillar Growth of Lithium–Titanate–Carbon Composite Structures by Self-Biased Direct Current Magnetron Sputtering for Lithium Ion Microbatteries

Jarkko Etula,* Katja Lahtinen, Niklas Wester, Ajai Iyer, Kai Arstila, Timo Sajavaara, Tanja Kallio, Ulf Helmersson, and Jari Koskinen

Here, an unidentified type of micropillar growth is described at room temperature during conventional direct-current magnetron sputtering (DC-MS) deposition from a $\text{Li}_4\text{Ti}_5\text{O}_{12}$ +graphite sputter target under negative substrate bias and high operating pressure. These fabricated carbon– Li_2O – TiO_2 microstructures consisting of various $\text{Li}_4\text{Ti}_5\text{O}_{12}/\text{Li}_2\text{TiO}_3/\text{Li}_x\text{TiO}_2$ crystalline phases are demonstrated as an anode material in Li-ion microbatteries. The described micropillar fabrication method is a low-cost, substrate independent, single-step, room-temperature vacuum process utilizing a mature industrial complementary metal–oxide–semiconductor (CMOS)-compatible technology. Furthermore, tentative consideration is given to the effects of selected deposition parameters and the growth process, as based on extensive physical and chemical characterization. Additional studies are, however, required to understand the exact processes and interactions that form the micropillars. If this facile method is further extended to other similar metal oxide–carbon systems, it could offer alternative low-cost fabrication routes for microporous high-surface area materials in electrochemistry and microelectronics.

1. Introduction

Direct current magnetron sputtering (DC-MS) is a mature industrial physical vapor deposition (PVD) method used to produce high-quality functional films for a diverse range of market sectors.^[1] Most of the scaling-related problems were overcome

in the early 1970s,^[2] with current research focusing, e.g., on further decreasing process times with various unbalanced magnetron sputtering techniques.^[3]

Magnetron sputtering can produce various kinds of films depending on a wide range of deposition parameters. In 1977 Thornton introduced Structure Zone models to describe different types of film growth as a function of deposition pressure and substrate temperature.^[4] The models were later suggested by Anders to also account for generalized homologous temperature, normalized kinetic energy flux, and net film thickness, only to name a few of the several primary physical parameters that can affect film growth.^[5] In the 1980s, sputtering at elevated working pressures was used to induce gas nucleation and particle agglomeration to deposit nanoparticles onto substrates.^[6] Subsequent high-pressure sputtering


setups to synthesize nanoparticles developed into so called cluster sources.^[7] This controllable, room temperature, and CMOS compatible method to deposit highly functional nanoparticles onto any desired surface has yielded several electrical, optical, and magnetic applications.^[8] In general, the inherently enormous surface area and microporosity offered by nanoparticles has been instrumental in advancing several electrochemical applications.^[9–11] One example is the Li-ion battery anode material demonstrated in this work, where higher sputtering pressures are employed to promote the nanostructuring of the electrode material.

The increasingly accelerated integration of low-current self-powered microelectronics in Internet-of-Things (IoT), such as wearable transmitters, sensors, and actuators requires microbatteries that are safe, reliable, and stable over a wide range of temperatures.^[12,13] One such material is the Li_2O – TiO_2 anode material system discussed in this work. The reader is suggested to refer to Kleykamp for the binary Li_2O – TiO_2 and ternary Li–Ti–O phase diagrams.^[14] $\text{Li}_4\text{Ti}_5\text{O}_{12}$, for example, is known for its high stability, safety, good rate-capability, and electronic conductivity at moderate current densities.^[15,16] Addition of carbon into the electrodes as a conductive agent is a common way to further

J. Etula, K. Lahtinen, N. Wester, Dr. A. Iyer, Prof. T. Kallio, Prof. J. Koskinen
Department of Chemistry and Materials Science
Aalto University School of Chemical Engineering
02150 Espoo, Finland
E-mail: jarkko.etula@aalto.fi

Dr. K. Arstila, Prof. T. Sajavaara
Department of Physics
University of Jyväskylä
40500 Jyväskylä, Finland

Prof. U. Helmersson
Department of Physics
Linköping University
SE-581 83 Linköping, Sweden

 The ORCID identification number(s) for the author(s) of this article can be found under <https://doi.org/10.1002/adfm.201904306>.

DOI: 10.1002/adfm.201904306

improve on these properties, and the introduction of micro-porosity as nanostructuring has been also shown to be effective, as reviewed by Liu and Cao.^[15] In lithiation by intercalation, the diffusion of the Li-ion in the electrolyte is followed by the electrochemical reaction at the electrode electrolyte interphase, further followed by diffusion into the bulk. Therefore, open microporous networks of nanostructures offer higher power densities, shorter diffusion and intercalation distances, as well as high pseudocapacitive contributions to charge storage.^[17,18] Whereas $\text{Li}_4\text{Ti}_5\text{O}_{12}$ is known as a zero-strain material during lithium insertion,^[19] anatase and rutile TiO_2 can exhibit lattice expansion and strain.^[20,21] Through nanostructuring, however, this expansion can be accommodated, potentially improving energy density and cyclability.^[20]

In literature, Wang et al. describe the deposition of crystalline $\text{Li}_4\text{Ti}_5\text{O}_{12}$ thin films for microbattery applications using radio frequency magnetron sputtering (RF-MS) at in situ temperatures of 500–700 °C.^[22] Since $\text{Li}_4\text{Ti}_5\text{O}_{12}$ by itself as a sputtering target is too resistive, it requires RF-MS, which suffers from high equipment costs and low deposition rates. A similar study by Wunde et al. utilized ion-beam sputtering at temperatures of 475–600 °C to fabricate $\text{Li}_4\text{Ti}_5\text{O}_{12}$ thin films for Li-ion storage.^[23]

To improve on these previous studies, the current work introduces i) a composite target consisting of $\text{Li}_4\text{Ti}_5\text{O}_{12}$ and graphite powder. This makes the target more conductive, enabling the use of DC-MS, which is considerably cheaper, simpler, and enables higher deposition rates due to higher currents at lower target voltages. ii) The added carbon also becomes mixed into the final electrode structure, enhancing electrochemical performance and electrical conductivity,^[15] as well as promoting structural diversity and nanocrystallinity. iii) A hydrated microporous multiphase carbon– Li_2O – TiO_2 pillar structure achieved at room temperature using a combination of substrate self-biasing and higher process gas pressures. As reported by Wang et al.,^[24] a hydrated Li_2O – TiO_2 multiphase structure was recently found to sustain more than 10 000 cycles with capacity fade of only 0.001% per cycle.

In this work we describe a method enabling a new and yet unreported type of micropillar growth of LTO-Carbon (LTO-C) nanocomposite structures at room temperature using conventional DC-MS deposition under higher than normal operating pressures and a negative substrate bias. The electrochemical performance and applicability of these high surface area microstructures is briefly demonstrated in Li-ion microbatteries. The physical properties and the elemental composition are also extensively characterized to shed light on the growth process. In contrast to more elaborate synthesis schemes, this work combines the electrically conductive amorphous carbon, high surface area, and intrinsic micropillar patterning at room temperature into a single process step utilizing a conventional industrial technology.

To the best of our knowledge, the room temperature deposited LTO-C micropillar structure, the mechanism of the micropillar growth, or the possible self-assembly of nanoparticles during DC-MS reported here is widely unidentified in literature. Similar structures can be usually prepared by using for example nanolithography and patterning,^[25,26] or by using nanoparticles as a template for reactive ion etching (RIE).^[27] Also processes at elevated temperatures, such as the plasma-enhanced chemical

vapor deposition (PECVD) of carbon nanofibers (CNF),^[28] allow the fabrication of similar 3D structures for a variety of electrochemical applications.

2. Results and Discussion

2.1. Physical Characterization

2.1.1. Microscopy

Helium ion microscopy (HIM) in **Figure 1a–d** and scanning electron microscopy (SEM) in **Figure 1e–g** were carried out to investigate the deposited LTO-C pillar structures. **Figure 1** shows representative micrographs from the surface of the LTO-C structure.

On the aluminum (**Figure 1a–e**), the pillars are well distributed, however, with some areas of lower pillar density. Growth on the Si-wafer (**Figure 1f–g**) is more uniform and there are also smaller pillars present. On both substrates there has also grown a thin film on the bottom (**Figure 1e,f**). Cross-sections of LTO-C pillars milled by focused ion beam (FIB) in **Figure 1c** shows that the pillars contain voids. Vertical line-artifacts produced by FIB-milling are also visible. The average size of the larger visible voids in **Figure 1c** is around 9 ± 3 nm ($N = 46$, standard deviation). It is unclear if these voids are open or closed, and if they contribute to the electrochemical performance of the material. Overall, LTO-C pillar growth is observed on several substrates: aluminum foil native oxide surface, P+ boron-doped (100) Si-wafer native oxide surface, and TiN films grown on same Si-wafers (**Figure S1**, Supporting Information). An approximate number density for pillars grown on each substrate is computed using image processing from SEM images provided in **Figure S2**, Supporting Information. The densities are 1.30 pillars μm^{-2} for aluminum foil, 1.94 pillars μm^{-2} for Si-wafer, and 2.40 pillars μm^{-2} for the sputter grown TiN film on same Si-wafer.

It is apparent from **Figure 1** and **Figure S2** in the Supporting Information that the pillar growth is more homogenous on the silicon wafer than on the aluminum foil. This is likely due to the more inhomogeneous surface morphology and chemistry of the aluminum surface that gives rise to an inhomogeneous electrical signature of the surface. For both substrates, but more pronounced on the silicon, the pillars start to grow with a high areal density, but due to competitive growth, the number density decreases as the pillars become higher. The observation that the pillar surfaces are rough, and they contain voids is comparably different from the more homogenous surface layer formed directly on the substrate. This may indicate that the pillars are formed of nanoparticles formed in-flight (**Figure 1b**), as sputtered species may nucleate into nanoparticles when sufficiently cooled by, e.g., process gases in the vacuum chamber.

Alternatively, while the sputtered LTO-C species are expected to have low surface mobility due to high gas pressure and room temperature process conditions, the pillar structure could be affected by plasma interaction and localized heating as evidenced by the high floating potential during deposition. Sponge-like morphology has been reported for sputtered films of Ni, Al, Ag, and Au, although at high surface mobility conditions and elevated process temperatures corresponding $\approx 0.5 T_{\text{melt}}$.^[29] Bunting et al.

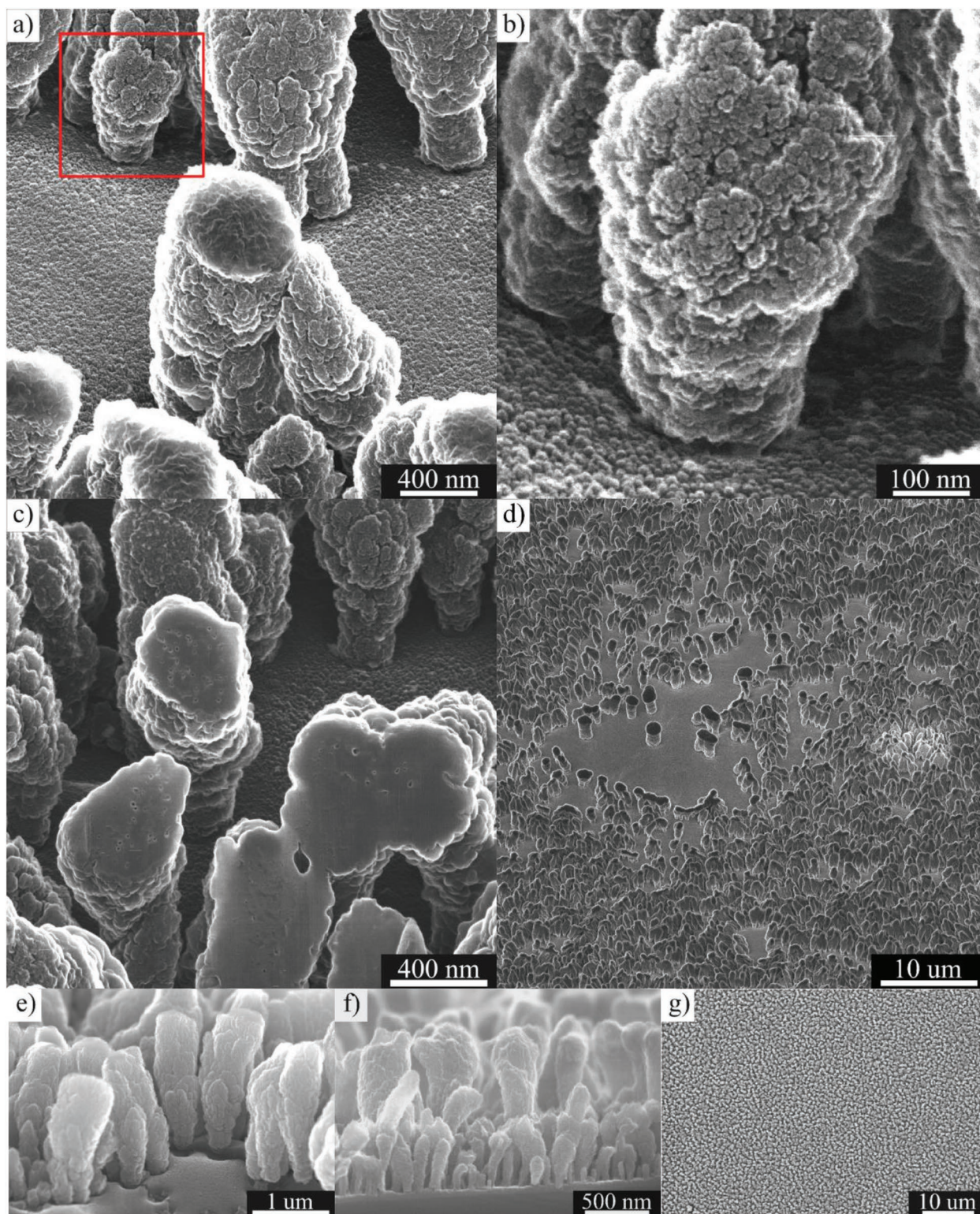


Figure 1. Micrographs of the LTO-C pillars grown on a–e) aluminum foil, and f–g) silicon wafer. b) Magnified highlight of the red box marked in (a). c) Cross-sections of pillars containing voids, milled by FIB. a–d) Helium ion microscope, and e–g) scanning electron microscope.

report the formation of similar 3D structures during RF-sputtering of LiFePO_4 +graphite,^[30] but likewise at elevated process temperatures of 600 °C and at deposition times of 4 h, since only film

was obtained prior to 1–2 h. Bünting et al. also only provide X-ray diffraction (XRD) analysis of crystalline phases for the elemental composition.^[30] Therefore, to better understand the elemental

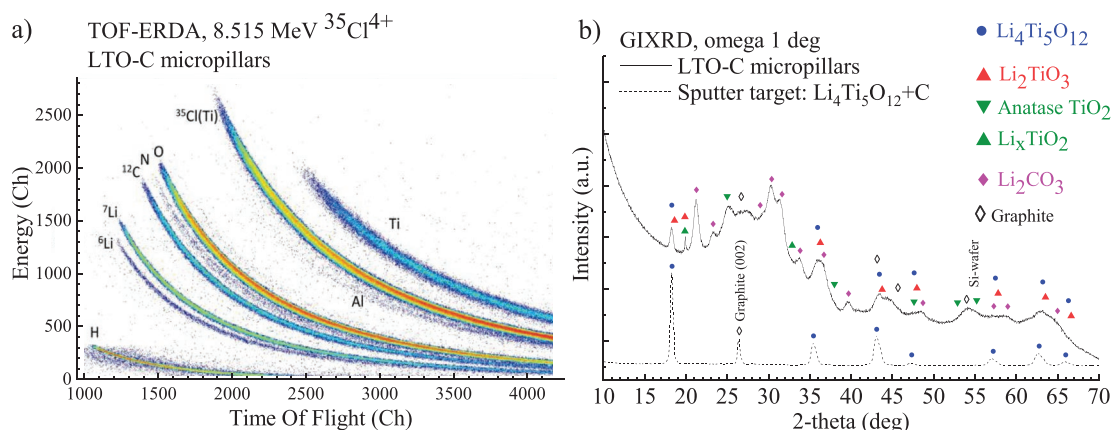


Figure 2. a) TOF-ERDA experimental results of the LTO-C pillars in a raw histogram depicting time-of-flight versus energy, b) glancing angle X-ray diffraction 2θ scans of the LTO-C pillars and of the initial sputter target material ($\text{Li}_4\text{Ti}_5\text{O}_{12}$ +graphite) at an incidence angle of 1° . Not all minor peaks are labeled; see Figure S3 in the Supporting Information for details.

composition of LTO-C pillars fabricated in current work, time-of-flight elastic recoil detection analysis (TOF ERDA) was carried out (Figure 2a) to obtain a complete elemental profile.

2.1.2. Time-Of-Flight Elastic Recoil Detection Analysis

Figure 2a and Table 1 display the elemental composition of the LTO-C pillars as measured by TOF-ERDA. Compared to the expected stoichiometry of the target material ($\text{Li}_4\text{Ti}_5\text{O}_{12}$), the LTO-C structure is richer in lithium, and oxygen, with possible hydrates and carbon originating from the graphite powder and water residues. The elemental depth distribution is consistent (Figure S4, Supporting Information).

2.1.3. Raman and Infrared Spectroscopy

Attenuated total reflection Fourier-transform infrared spectroscopy (ATR FTIR) (Figure 3a) was carried out to obtain a broader perspective on the types of bonding present in the LTO-C pillars. The spectrum displayed in Figure 3a shows a broad absorption band in the range of 3600 to 2780 cm^{-1} , evidencing presence of adsorbed $-\text{OH}$ groups. Two additional peaks centered at 2850 and 2921 cm^{-1} were also observed. These bands have previously been observed for amorphous carbon (a-C) coatings and are frequently attributed to $-\text{CH}$ stretching of $-\text{CH}_3$ groups.^[32] a-C residues can be also found as carbonaceous impurities in $\text{Li}_4\text{Ti}_5\text{O}_{12}$.^[33] The presence of a-C could further explain the relatively broad shoulder of the 1502 cm^{-1} peak due to $\text{C}=\text{C}$ stretching, $\text{C}=\text{O}$ stretching, and $\text{C}-\text{O}$ in the amorphous carbon.^[32]

Table 1. TOF-ERDA elemental compositions as calculated from the area marked with dotted lines in Figure S4 in the Supporting Information. The given uncertainties include both statistical uncertainties and uncertainties due to ion beam irradiation induced losses during the measurement.

Sample	Li [at%]	O [at%]	Ti [at%]	N [at%]	C [at%]	H [at%]
LTO-C	17 ± 1	52 ± 3	11 ± 1	0.7 ± 0.1	12 ± 2	9 ± 1

Peaks attributed to Li_2CO_3 can be seen centered at 1605 , 1500 , 1421 , 1085 , 861 , and 490 cm^{-1} . In the lower wavenumber region, several broad peaks that could be attributed to both Li_2CO_3 and $\text{Li}_4\text{Ti}_5\text{O}_{12}$ are found. Additional expected bands of medium or weak intensity for Li_2CO_3 at 360 , 410 , 440 , 713 , and 740 cm^{-1} have also been observed.^[34,35] These bands could explain the broad peaks in the range of 712 – 790 cm^{-1} and to the broad shoulder of the peak center around 490 cm^{-1} . The broad peak centered around 650 cm^{-1} is likely due to symmetric stretching vibration of TiO_6 ,^[33] and have been previously observed for $\text{Li}_4\text{Ti}_5\text{O}_{12}$.^[33,36] The second expected band for antisymmetric TiO_6 stretching is likely also present, but overlaps with bands for Li_2CO_3 , and could, therefore, not be assigned. It should also be noted that peaks in the range 440 and 500 – 600 cm^{-1} have previously been attributed to $\text{Ti}-\text{O}$ and $\text{Li}-\text{O}$ modes, respectively.^[33]

Raman spectroscopy in Figure 3b confirms the presence of amorphous carbon, as indicated by i) a broad D-peak, ii) a sharper G-peak at around 1585 cm^{-1} , and iii) high I_D/I_G peak intensity ratio of 2.6, as per Ferrari and Robertson (Figure S5, Supporting Information).^[31,37] Figure 3b also shows the presence of Li_2CO_3 in a sharp peak at 1087 cm^{-1} ,^[34,35] a collection of peaks in the range of 90 – 190 cm^{-1} , and a sharp peak at 1486 cm^{-1} .^[35] Three broad peaks centered around 236 , 431 , and 666 cm^{-1} likely attributed to $\text{Li}_4\text{Ti}_5\text{O}_{12}$ were also observed and are assigned in Figure 3b, indicating presence of $\text{Li}_4\text{Ti}_5\text{O}_{12}$. Kellerman et al. showed that carbon coating shifts the peaks to lower wavenumbers, as observed also in this work with the main strong lines for $\text{Li}_4\text{Ti}_5\text{O}_{12}$.^[38] It should be noted that the broad peaks may also indicate overlapping peaks for Li_2TiO_3 or TiO_2 .^[39,40]

The FTIR and Raman analysis in Figure 3 indicate the presence of amorphous carbon, Li_2CO_3 , $\text{Li}_4\text{Ti}_5\text{O}_{12}$, and possibly Li_2TiO_3 as well as TiO_2 . These results are in good agreement with the structural diversity of crystalline material observed in the XRD analysis (Figure 2b). Although there is no direct evidence to suggest a mechanism for the formation of Li_2CO_3 , it is possible that the excess lithium left over from the vacuum process reacts in the atmosphere to form Li_2CO_3 . This Li_2CO_3 , and additional hydrates as well as oxygen functionalities, may explain the high concentration of oxygen and hydrogen found by TOF-ERDA in Table 1, when compared only to the

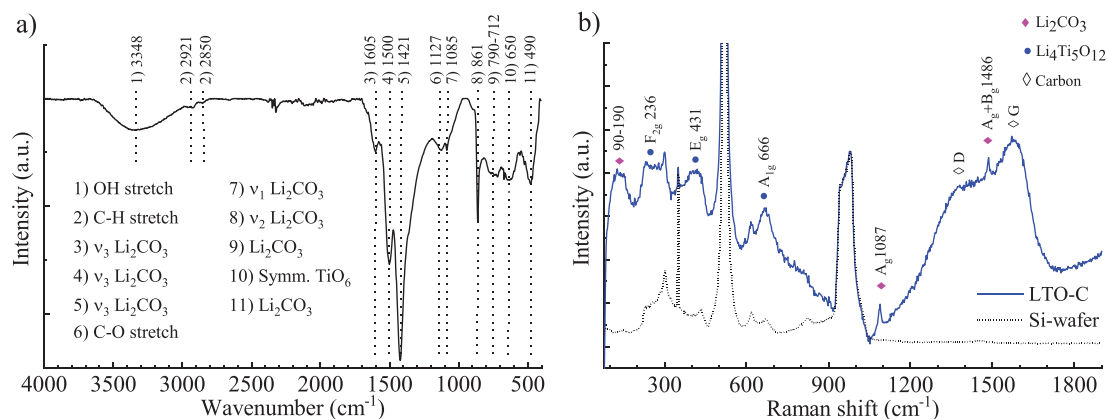


Figure 3. a) Attenuated total reflection Fourier-transform infrared spectroscopy (ATR FTIR) results as measured from the LTO-C pillars. b) Raman spectroscopy results of the LTO-C. The D and G peaks for amorphous carbon in (b) are fitted as described by Ferrari & Robertson in Figure S5 (Supporting Information).^[31]

stoichiometric composition of $\text{Li}_4\text{Ti}_5\text{O}_{12}$. It is, however, inconclusive whether any water is located within the LTO-C, in Li_2CO_3 , or on the surface as adsorbed water. Detailed NMR studies are required to investigate the bonding of water.

Overall, the FTIR and Raman observations are in line with the low process temperature and expected structural diversity, as further investigated by glancing angle X-ray diffraction (GIXRD) in Figure 2b. In literature it is suggested by Rahman et al. that amorphous carbon mixed within the nanostructure of $\text{Li}_4\text{Ti}_5\text{O}_{12}$ - TiO_2 would promote diversity and impede structural coarsening and grain growth.^[41] Additionally, since plain Li_2O - TiO_2 structures can be resistive, amorphous carbon is commonly added to electrode structures to promote conductivity, facilitate lithium insertion/removal, provide structural stability, and minimize trapping sites.^[41] It is, therefore, expected that the amorphous carbon found in the LTO-C pillars in Figure 3b can enhance electrochemical performance in rate capability, cycling life, and capacity retention.^[42,43]

2.1.4. Glancing Angle X-Ray Diffraction

GIXRD was carried out (Figure 2b) to identify phases present in the LTO-C pillars. Silicon wafer diffraction peaks have been documented in the same GIXRD setup in previous work.^[44] The scan shown in Figure 2b indicates the presence of multiple Li_2O - TiO_2 phases at $18.5^\circ 2\theta$, likely a mix of β - Li_2TiO_3 (COD 96-151-5996) and $\text{Li}_4\text{Ti}_5\text{O}_{12}$ (96-100-1099). There are also several possible TiO_2 polymorphs at 20.2° and $25.3^\circ 2\theta$, which could be lithiated. The wide Li_2O - TiO_2 phase diffraction peaks in Figure 2b indicate crystallinity in the nanoscale range, as per Scherrer equation. More definite phase identification and crystallite size approximation are, however, hindered by peak convolution due to presence of Li_2CO_3 (96-900-9643) and an apparent wide carbon background around $26^\circ 2\theta$. Higher angle 2θ peaks are also broadened by the large beam footprint of the surface sensitive asymmetric 1° incidence angle, as also seen in the scan for the sputter target material ($\text{Li}_4\text{Ti}_5\text{O}_{12}$ +graphite). See Figure S3 in the Supporting Information for detailed peak positions of all phases.

The nanoscale crystallinity found in Figure 2b agrees with the porous pillar structures observed by HIM and SEM in Figure 1. Also, the crystalline phase composition agrees with the binary Li_2O - TiO_2 phase diagram by Kleykamp,^[14] as TOF-ERDA indicates that the stoichiometry is Li_2O -rich compared to $\text{Li}_4\text{Ti}_5\text{O}_{12}$ stoichiometry, i.e., composition of $\text{Li}_2\text{TiO}_3/\text{Li}_4\text{Ti}_5\text{O}_{12}$. This suggestion, however, is in contrast to the apparent presence of an anatase TiO_2 phase, but it can be also explained with the room temperature process and the presence of possible hydrates, similar to those observed in water-based synthesis intermediates.^[24]

In literature, Wang et al. prepared crystalline $\text{Li}_4\text{Ti}_5\text{O}_{12}$ films by RF sputtering at 500 – 700°C in low pressures (no added carbon).^[22] Even 500°C in situ annealing resulted in $\text{Li}_4\text{Ti}_5\text{O}_{12}$ films of low crystallinity. Since the method used in the present work is carried out at room temperature, the wide peaks and low crystallinity of Li_2O - TiO_2 phases found in Figure 2b are as expected but may not reflect the actual amounts of more amorphous electrochemically active structures.

There are several inherent benefits for both mechanical as well as electrochemical properties in Li-ion storage when utilizing a diverse nanocrystalline network consisting of different functional phases. i) A nanocrystalline TiO_2 structure can have a higher amount of surface defects and interfaces which enhance the potential Li-ion storage capacity and kinetics.^[15,18] ii) Wang et al. found that structural diversity induced by hydrates in Li_2O - TiO_2 - H_2O systems can be highly beneficial for the battery performance in aprotic electrolytes, since complete dehydration and annealing would coarsen the structure and degrade both cyclability and electrochemical performance.^[24] Similarly, it has been found that for example multiphase $\text{Li}_2\text{TiO}_3/\text{Li}_4\text{Ti}_5\text{O}_{12}$ composites can outperform pristine $\text{Li}_4\text{Ti}_5\text{O}_{12}$.^[45] Further, studies have found that each polymorphic form of TiO_2 : anatase, rutile, $\text{TiO}_2(\text{B})$, and brookite all have attractive lithium storage behaviors, especially when nanostructured.^[17,46]

2.2. Selected Deposition Parameters

Due to the high number of experimental variables, any discussion related to effects of deposition parameters should

be considered tentative pending further investigation. The described method was found to result in the formation of micropillars when i) a high working pressure of 60 mTorr argon, and ii) a substrate bias of -5 V with respect to ground were applied.

During the deposition, an accumulation of a negative electrical potential is measured between the substrate and ground at floating potentials, corresponding to a current of hundreds of milliamperes at -5 V bias. Considering for example the work by Bohlmark et al.,^[47,48] it is contemplated that although the target-to-substrate distance (8 cm) in this work is longer than that of the measured magnetron null point (5 cm), the substrate may be subjected to plasma interaction and heating localized to the top surface layers. It should be noted, however, that the temperature of both the deposition chamber and the substrate holder remained below 22 °C throughout the deposition, as measured by integrated thermocouples. This is expected from the work of Martin et al.,^[49] where DC-MS deposited TiO_2 films grown at a low pressure of 1 mTorr are submitted to a higher intrinsic ion bombardment than those deposited at a higher pressure of 11 mTorr.

High lithium mobility and segregation on sputter targets is commonly documented, as outlined for example by Dudney et al.^[50] This is, however, not often discussed in literature relating to sputtering of $\text{Li}_4\text{Ti}_5\text{O}_{12}$. Therefore, the high lithium content in the LTO-C pillar structures in this work may be due to i) segregation of lithium on the target during sputtering to form areas of higher and lower lithium contents across the sputtering target, or ii) different element-specific sputter yields depending on structural and compositional variations across the sputter target. Such effects may result in the formation of $\text{Li}_2\text{O-TiO}_2$ species of varying lithiation. This idea is also indicated in the contrast of TOF-ERDA results to those of XRD (Figure 2 and Table 1), where the $\text{Li}_2\text{O-TiO}_2$ stoichiometry is found elementally titanium-deficient, i.e., composition of $\text{Li}_2\text{TiO}_3/\text{Li}_4\text{Ti}_5\text{O}_{12}$, but there still appear TiO_2 phases in the XRD analysis.

As per the Structure Zone-model developed by Thornton,^[4] and later revised by Anders,^[5] the sputtering parameters used in this work would belong to the Zone 1. The Zone 1 structure results from very low incident atom energy, low surface mobility, and insufficient available energy for diffusion. This can result in shadowing effects and structures where nucleation occurs preferentially on substrate high points. As described by Sanzaro et al.,^[51] a glancing or oblique angle deposition based on the shadowing effect can be used to deposit, e.g., slanted pillars of TiO_2 . This small incidence angle, however, also significantly decreases deposition rate. In the current work, incidence angle is perpendicular to substrate, and the fairly large 4" target is at a distance of 8 cm. These factors are expected to minimize any shadowing effects, although it can be difficult to completely neglect an oblique flux due to effects of high gas pressure. Hence, as it appears from the interpillar separation in Figure 1, the LTO-C micropillar growth cannot be directly explained with shadowing effects or Thornton's structure zone models. Moreover, because pillar growth did not occur at grounded or floating potentials within the current experimental setup, a plasma interaction component may be involved. The beforehand mentioned study regarding the DC-MS deposition of TiO_2 by Martin et al. found the flux and mean energy of positive ions to decrease as the pressure increased.^[49] For O^- species on

the other hand, the mean energy and flux of O^- was inversely affected by the total pressure for it to become the dominant ion flux by an order of magnitude with a mean energy of 27 eV at 11 mTorr Ar pressure.^[49]

Another important parameter is the possibility of gas phase nucleation occurring at the 60 mTorr argon gas pressure and 8 cm working distance as used in this paper, selected based on the work of Gunnarsson et al. for TiO_2 .^[52] For example, Geetha Priyadarshini et al. have investigated the effects of substrate bias, gas pressure, and deposition temperature of TiO_2 , but have neither used similar bias ranges nor high enough gas pressures.^[53] Also, most methods apply substrate temperatures of $400\text{--}600$ °C to enhance crystallization and stoichiometry using, e.g., RF-sputtering or ion-beam sputtering of $\text{Li}_4\text{Ti}_5\text{O}_{12}$.^[22,23,30] Few to no studies can be found on sputtering of lithiated titania at room temperature with substrate biasing and higher gas pressures.

2.3. Electrochemical Characterization

The cyclic voltammogram of the LTO-C micropillars, presented in Figure 4a, shows broad peaks for both the anodic and cathodic intercalation process. Two peaks can be observed for each, especially in the 0.1 mV s^{-1} scan rate, two anodic peaks being located at 1.72 and 1.94 V. This indicates the presence of two or more Li-extraction processes occurring at different potentials. The 1.72 V peak corresponds to the lithium intercalation reaction of $\text{Li}_4\text{Ti}_5\text{O}_{12}$, and the 1.94 V to that of some TiO_2 polymorph. However, due to peak convolution, the characteristic Li-extraction processes cannot be reliably identified.

As determined by XRD in Figure 2b, the LTO-C pillars were rich in a number of different $\text{Li}_2\text{O-TiO}_2$ phases, each likely contributing to the overall extraction process. A significant portion of the crystalline material consists of Li_2CO_3 , which is electrochemically inert and is not expected to contribute to Li-ion storage capacity.^[54] Furthermore, due to low density and irregular distribution of pillars on aluminum foil (Figure 1), it is difficult to estimate the actual amount of electroactive storage material to determine appropriate currents for rate capability measurements shown in Figure 4b,c. The lowest and highest current densities (Figure 4b,c) were approximated to correspond to C-rates of 0.1 C and 10 C, assuming the LTO-C electrode is 50% covered by 1.5 μm tall pillars composed of only $\text{Li}_4\text{Ti}_5\text{O}_{12}$.

The initial specific capacity during discharge (Figure 4b) is ≈ 27 $\mu\text{Ah cm}^{-2}$ at 2.2 $\mu\text{A cm}^{-2}$, and it decreases significantly after the first cycle to ≈ 25 $\mu\text{Ah cm}^{-2}$. With the current increasing, the specific capacity drops to ≈ 22 $\mu\text{Ah cm}^{-2}$ at 22.6 $\mu\text{A cm}^{-2}$, and 16 $\mu\text{Ah cm}^{-2}$ at 227.4 $\mu\text{A cm}^{-2}$. In other words, the 227.4 $\mu\text{A cm}^{-2}$ capacity is ≈ 64 % of the initial capacity at 2.2 $\mu\text{A cm}^{-2}$, which is still rather high. Three cycles were performed with all currents to test the stability of the cell. As seen in Figure 4c, the three subsequent cycles of any current give very similar specific capacities indicating that the half-cells are stable. To further investigate the stability and to tentatively investigate the cycle life of the cell, after the 227.4 $\mu\text{A cm}^{-2}$ cycles three more cycles with 4.5 $\mu\text{A cm}^{-2}$ were performed. While the

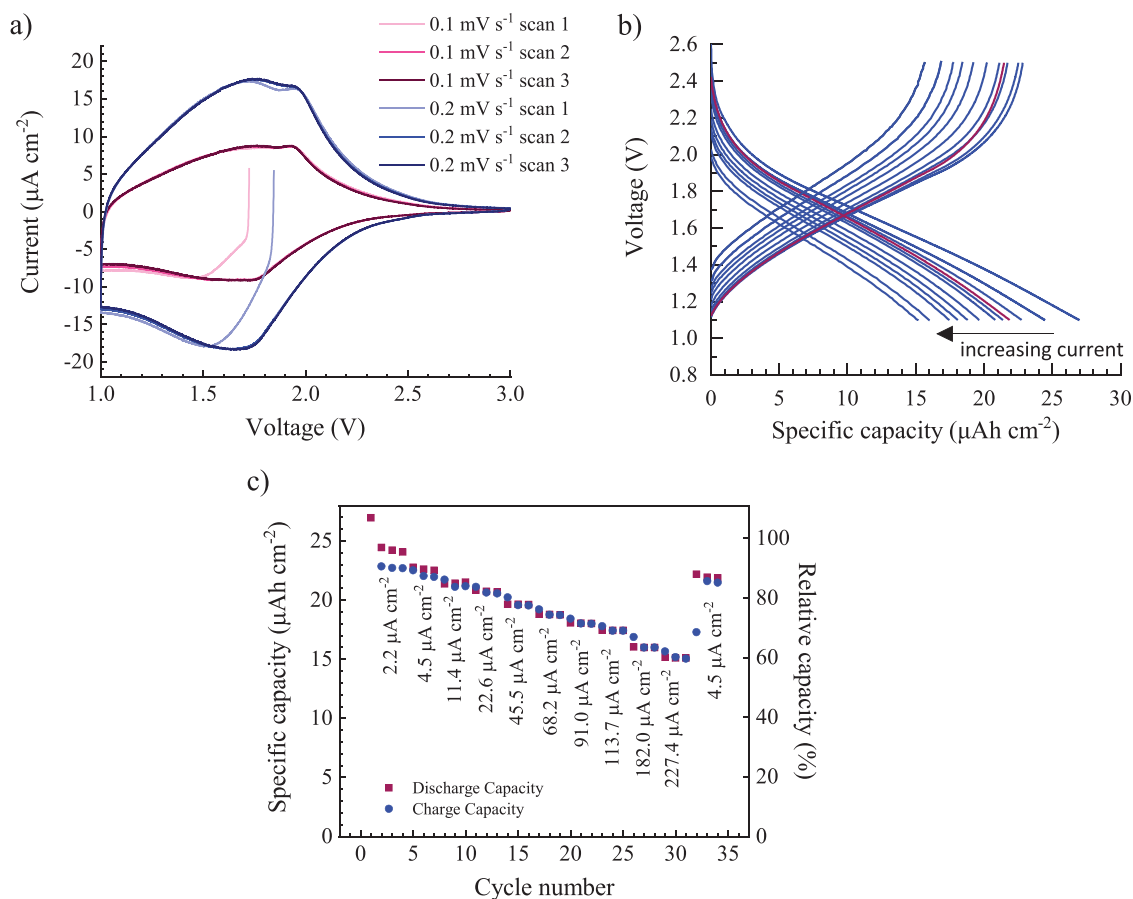


Figure 4. a) Cyclic voltammetry curves of LTO-C micropillars on aluminum foil at scan rates of 0.1 and 0.2 mV s^{-1} in the voltage range of 1.0–3.0 V. b) and c) Electrochemical Li-insertion rate capability results. The lowest and highest current densities were approximated to correspond to C-rates of 0.1 C and 10 C. The red line in b) corresponds to the last scan ($N = 35$) performed at 0.2 C ($4.5 \mu\text{A cm}^{-2}$).

initial $4.5 \mu\text{A cm}^{-2}$ cycles give a capacity of $22.7 \mu\text{Ah cm}^{-2}$, the final $4.5 \mu\text{A cm}^{-2}$ give a capacity of $22.1 \mu\text{Ah cm}^{-2}$. The drop is small (97.4% retained capacity) and indicates good cyclability for the cell. Obviously, an actual life cycle measurement should be performed to fully demonstrate the lifetime of this material, but the scope of this section is only to investigate and compare the electrochemical characteristics of the LTO-C composite to physical characteristics.

The initial capacity of the cell is quite low compared to typical values reported for microbatteries, for example, $1\text{--}1.2 \text{mAh cm}^{-2}$ for 3D-printed macroscopic electrodes.^[55,56] This is, however, expected since the LTO-C pillars are only roughly $1.5 \mu\text{m}$ tall and the growth density is only around $1.3 \text{pillars } \mu\text{m}^{-2}$ on aluminum foil (Figure 1 and Figure S2, Supporting Information). If the volume of LTO-C material on substrate is approximated by assuming a 50% surface coverage by $1.5 \mu\text{m}$ tall pillars ($\mu\text{Ah cm}^{-2} \mu\text{m}^{-1}$), this would approximately correspond to values reported by Wang et al. for $\text{Li}_4\text{Ti}_5\text{O}_{12}$ thin films of similar volume deposited at 500°C .^[22]

Although the presence of Li_2CO_3 in the LTO-C structure appears undesired, it has been reported by Bhattacharya et al. that a Li_2CO_3 surface coating of graphite anodes can reduce structural damage and improve long term cycling capacity with certain electrolytes by reducing solvent co-intercalation induced

surface damage.^[57] Their work involved attaching Li_2CO_3 particles to electrode surfaces from solutions with Agar as an adhesion promoter, whereas in the current work this appears to be intrinsic to the chosen deposition parameters.

3. Conclusion

An unidentified type of micropillar growth was discovered during conventional DC-MS deposition from a $\text{Li}_4\text{Ti}_5\text{O}_{12}$ +graphite sputter target at room temperature under relatively high operating pressures and a negative substrate bias. A simple type of substrate self-biasing was achieved using a variable resistor to ground the substrate. Based on physical and electrochemical characterization, the resulting carbon– Li_2O – TiO_2 structures were found to have several functional properties toward application as anode material in Li-ion microbatteries. Furthermore, effects of used deposition parameters were tentatively discussed based on the physical characteristics of the deposited LTO-C pillars. Both the high argon gas pressure of 60 mTorr and the relatively low negative substrate bias of -5V w.r.t. ground was found critical for pillar growth.

Compared to, e.g., more elaborate high temperature processes, the described micropillar fabrication method is

low-cost, single-step, room-temperature vacuum process utilizing a mature CMOS compatible industrial technology. The customizability of the DC-MS process also offers additional possibilities in modifying the pillars, e.g., by N_2 , O_2 , or H_2O doping to obtain a desirable electrical or electrochemical response.

Additional studies are, however, required to better understand and develop this novel type of micropillar or fiber growth. If this facile fabrication method can be further extended to other metal oxide–carbon systems, it could enable the emergence of alternative low-cost fabrication routes for high-surface area electrode materials in electrochemistry and microelectronics.

4. Experimental Section

Prior to methods detailed below, an effort was made to deposit carbon-coated, hydrated, and highly porous LTO-C films at high argon pressures, which yielded highly unexpected bush-like surface structures (Figure S6, Supporting Information). These substrates were mounted on an electrically grounded holder using conductive carbon tape (Ted Pella). Although unrecorded, the effective resistivity of the grounding connection was estimated to be low. This result prompted a further investigation of deposition parameters, such as the self-biasing described in this work. It is also contemplated that several deposition parameters, such as the deposition rate and addition of reactive gases such as nitrogen, can affect the dimensional properties of the grown pillars.

DC-MS Deposition of LTO-C Pillars: The custom 4" diameter lithium titanate graphite target was prepared by drop casting 2 mL of solution consisting of (0.2 g) of LTO powder ($Li_4Ti_5O_{12}$, Sachtleben Pigments, Hombitec LTO5, P33583, 1 μm crystallite size) and 0.015 g of graphite (Alfa Aesar, 2–15 μm , 99.9995%) in ethanol onto a standard 4" Dia. \times 0.250" Thick graphite target (Kurt J. Lesker, 99.999%). The target was allowed to dry in a fume hood for 1 h after which it was further dried on a hotplate at 100 $^{\circ}C$ for 15 min to remove excess water. Some left-over water was expected, which was reported to be potentially beneficial for the electrochemical performance.^[24] The vacuum chamber was evacuated to a base pressure below 1×10^{-6} Torr using a CTI cryogenics CTI 8F cryopump prior to deposition.

The conventional DC magnetron sputter deposition (DC-MS) was carried out perpendicular to the substrate with an unmodified circular 4" TORUS (Kurt J. Lesker) DC-MS, at an anode-to-substrate distance of 80 mm. The magnetic field null point was measured to be at around 5 cm from the anode surface with a Hall effect probe. Depositions were run for a total of 60 min in 60 mTorr Ar pressures at a flow rate of 6 sccm Ar with an Edwards Vacuum XDS 15 dry scroll pump and a DC02 BP (Kurt J. Lesker) power source controlled by built-in KJL software. A run-in period of 4 min was used to ramp-up the freshly prepared LTO-C target to the target power of 700 W. DC power source output values were 504 V/1.38 A in the beginning of the deposition at 700 W, and 500 V/1.39 A at 60 min. The distance between the anode and dark-space shield was about 1.2 mm. This deposition power and time would correspond to a film around 1.2 μm thick at 5 mTorr Ar deposition pressure and grounded substrate.

A glass-plated (electrically insulated) substrate holder was used on which aluminum foil and Si (100) P+ (boron-doped, <0.005 Ohm cm) pieces were mounted using conductive carbon tape (Ted Pella). The electrically insulated substrates were grounded through a variable resistor: This allowed control over the charge accumulated on the substrate, i.e., self-biasing. A parallel voltmeter monitored this self-biasing potential between the substrate and the ground. During deposition, the variable resistor was controlled to maintain a bias potential of -5 V between the sample and the ground. A fully floating substrate in open-circuit would accumulate a negative bias of about -25 V. Current through the variable resistor was initially about 240 mA but decreased steadily to tens of milliamperes at the end of the

deposition. Samples were also prepared at both floating and grounded potentials, but these both resulted in flat thin films, as observed by SEM.

Physical Characterization: Glancing angle X-ray diffraction measurements were performed in parallel beam mode using a Rigaku SmartLab diffractometer equipped with a 9 kW rotating Cu anode and a 2 \times Ge(220) monochromator ($K\alpha_1$, 0.154 nm), HyPix-3000 2D single photon counting detector in 1D mode, 5 $^{\circ}$ Soller slits at both incident and detector ends, as well as incident slits of 0.1 mm vertical and 15 mm horizontal. GIXRD scans were acquired in asymmetric geometry with a fixed incidence omega angle of 1 $^{\circ}$. Scans were obtained for both LTO-C micropillars as well as for the sputter target material consisting of $Li_4Ti_5O_{12}$ mixed with graphite.

Visible-Raman spectroscopy was performed on a Horiba Jobin-Yvon Labram HR confocal Raman system with a 488 nm argon laser with 10 mW power on sample. A spot size of 1 μm was used with an Olympus 100 \times objective. Raman spectra were acquired in the range of 50 to 3000 cm^{-1} with a 600 lines/inch diffraction grating, exposure time of 15 s, and accumulation averaging count of two. Spectroscopic calibration was performed on intrinsic Si wafer (Ultrasil). Raman spectra were obtained from three places and fitted by two Gaussian peaks for D and G regions of amorphous carbon to obtain the I_D/I_G peak intensity ratios, as explained in literature.^[31]

ATR measurements were carried out using a Bruker FTIR ALPHA II spectrometer with a platinum ATR sampling module (diamond) in the spectral range of 400–4000 cm^{-1} .

Cross-sectional scanning electron microscopy analysis of the samples was performed with a Hitachi S-4700 SEM equipped with a field emission electron source operated at 15 kV accelerating voltage. Number density of the larger pillars grown on each substrate was computed using Gwyddion 2.50 software from 2k magnification planar SEM images by grain analysis and excluding grains less than 20 pixel² in size.

Surface morphology of LTO-C was studied with a Zeiss Orion Nanofab helium-ion microscope (HIM) at the Nanoscience Center of the University of Jyväskylä.

Elemental depth profiles of the LTO-C pillar structure were measured using a time-of-flight recoil detection analysis system (TOF-ERDA). A detailed description of the method and apparatus can be found in literature.^[58] The ion beam was a 8.515 MeV $^{35}Cl^{4+}$ from the 1.7 MV Pelletron accelerator at the Accelerator Laboratory of the University of Jyväskylä. Tilt angle was 20 $^{\circ}$ relative to the ion beam direction. Data was analyzed using Potku software.^[59]

Electrochemical Characterization: 14 mm diameter electrodes were cut from the LTO-C coated aluminum foil. The electrodes were assembled to Hohen 2016 coin cells in an argon atmosphere. Lithium metal foils (0.75 mm thick, Sigma-Aldrich) were used as a counter electrode in the half-cells. Lithium hexafluorophosphate ($LiPF_6$) dissolved in 1:1 ethylene carbonate (EC): dimethyl carbonate solution (DMC) was used as an electrolyte and Whatman GF/A (0.26 mm) filter paper as a separator. The cells were left to stabilize for 24 h before starting the electrochemical measurements.

Cyclic voltammetry (CV) of the half-cells was measured using Autolab potentiostat (PGSTAT302N) and a GPES software. The CVs were performed in the voltage range of 1.0–3.0 V versus Li/Li^+ using scan rates of 0.1 and 0.2 $mV s^{-1}$. Three cycles were recorded for both scan rates.

The rate capability measurements were performed using Neware battery cycler in the voltage range of 1.0–3.0 V versus Li/Li^+ . Three cycles with currents of 2.2, 4.5, 11.4, 22.6, 45.5, 68.2, 91.0, 113.7, 182.0, 227.4 $\mu A cm^{-2}$ were performed. Finally, the cells were cycled again three times with 4.5 $\mu A cm^{-2}$ to have initial information about the cycle life. The lowest and highest current densities were approximated to correspond to C-rates of 0.1 C and 10 C, assuming the LTO-C electrode is 50% covered by 1.5 μm tall pillars composed of $Li_4Ti_5O_{12}$.

Supporting Information

Supporting Information is available from the Wiley Online Library or from the author.

Acknowledgements

The authors acknowledge the provision of facilities by RawMatters Finland Infrastructure (RAMI, No. 292884) and OtaNano – Nanomicroscopy Center (Aalto-NMC). The authors wish to also thank Academy of Finland CloseLoop project (13303452).

Conflict of Interest

The authors declare no conflict of interest.

Keywords

amorphous carbons, batteries, lithium titanates, microstructures, porous materials

Received: May 29, 2019

Revised: July 11, 2019

Published online: August 12, 2019

- [1] P. S. McLeod, L. D. Hartsough, *J. Vac. Sci. Technol.* **1977**, *14*, 263.
 [2] R. K. Waits, *J. Vac. Sci. Technol.* **1978**, *15*, 179.
 [3] P. J. Kelly, R. D. Arnell, *Vacuum* **2000**, *56*, 159.
 [4] J. A. Thornton, *Annu. Rev. Mater. Sci.* **1977**, *7*, 239.
 [5] A. Anders, *Thin Solid Films* **2010**, *518*, 4087.
 [6] S. Iwama, K. Hayakawa, T. Arizumi, *J. Cryst. Growth* **1982**, *56*, 265.
 [7] L. Martínez, M. Díaz, E. Román, M. Ruano, D. Llamosa, P. Y. Huttel, *Langmuir* **2012**, *28*, 11241.
 [8] F. E. Kruis, H. Fissan, A. Peled, *J. Aerosol Sci.* **1998**, *29*, 511.
 [9] J. Wang, *Analyst* **2005**, *130*, 421.
 [10] R. W. Murray, *Chem. Rev.* **2008**, *108*, 2688.
 [11] B. R. Cuenya, *Thin Solid Films* **2010**, *518*, 3127.
 [12] Y. Wang, B. Liu, Q. Li, S. Cartmell, S. Ferrara, Z. D. Deng, J. Xiao, *J. Power Sources* **2015**, *286*, 330.
 [13] J. F. M. Oudenhoven, L. Baggetto, P. H. L. Notten, *Adv. Energy Mater.* **2011**, *1*, 10.
 [14] H. Kleykamp, *Fusion Eng. Des.* **2002**, *61–62*, 361.
 [15] D. Liu, G. Cao, *Energy Environ. Sci.* **2010**, *3*, 1218.
 [16] E. Pohjalainen, J. Kallioinen, T. Kallio, *J. Power Sources* **2015**, *279*, 481.
 [17] N. A. Kyeremateng, *ChemElectroChem* **2014**, *1*, 1442.
 [18] J. Haetge, P. Hartmann, K. Brezesinski, J. Janek, T. Brezesinski, *Chem. Mater.* **2011**, *23*, 4384.
 [19] T. Ohzuku, *J. Electrochem. Soc.* **1995**, *142*, 1431.
 [20] S. Bach, J. P. Pereira-Ramos, P. Willman, *Electrochim. Acta* **2010**, *55*, 4952.
 [21] B. J. Morgan, G. W. Watson, *Phys. Rev. B* **2010**, *82*, 144119.
 [22] C.-L. Wang, Y. C. Liao, F. C. Hsu, N. H. Tai, M. K. Wu, *J. Electrochem. Soc.* **2005**, *152*, A653.
 [23] F. Wunde, F. Berkeleier, G. Schmitz, *J. Power Sources* **2012**, *215*, 109.
 [24] S. Wang, W. Quan, Z. Zhu, Y. Yang, Q. Liu, Y. Ren, X. Zhang, R. Xu, Y. Hong, Z. Zhang, K. Amine, Z. Tang, J. Lu, J. Li, *Nat. Commun.* **2017**, *8*, 627.
 [25] Y. Paz, *Beilstein J. Nanotechnol.* **2011**, *2*, 845.
 [26] R. P. Seisyan, *Tech. Phys.* **2011**, *56*, 1061.
 [27] W.-L. Min, P. Jiang, B. Jiang, *Nanotechnology* **2008**, *19*, 475604.
 [28] T. Laurila, S. Sainio, H. Jiang, N. Isoaho, J. E. Koehne, J. Etula, J. Koskinen, M. Meyyappan, *ACS Omega* **2017**, *2*, 496.
 [29] A. F. Jankowski, J. P. Hayes, *J. Vac. Sci. Technol., A* **2003**, *21*, 422.
 [30] A. Bunting, S. Uhlenbruck, D. Sebold, H. P. Buchkremer, R. Vaßen, *ACS Appl. Mater. Interfaces* **2015**, *7*, 22594.
 [31] A. C. Ferrari, J. Robertson, *Phys. Rev. B* **2001**, *64*, 075414.
 [32] V. Jucureanu, A. Matei, A. M. Avram, *Crit. Rev. Anal. Chem.* **2016**, *46*, 502.
 [33] M. Senna, M. Fabián, L. Kavan, M. Zúkalová, J. Briančin, E. Turianicová, P. Bottke, M. Wilkening, V. Šepelák, *J. Solid State Electrochem.* **2016**, *20*, 2673.
 [34] P. Pasierb, S. Komornicki, M. Rokita, M. Rękas, *J. Mol. Struct.* **2001**, *596*, 151.
 [35] M. H. Brooker, J. B. Bates, *J. Chem. Phys.* **1971**, *54*, 4788.
 [36] M. W. Raja, S. Mahanty, M. Kundu, R. N. Basu, *J. Alloys Compd.* **2009**, *468*, 258.
 [37] A. C. Ferrari, J. Robertson, *Phys. Rev. B* **2000**, *61*, 14095.
 [38] D. G. Kellerman, V. S. Gorshkov, E. V. Shalaeva, B. A. Tsaryev, E. G. Vovkotrub, *Solid State Sci.* **2012**, *14*, 72.
 [39] R. Ramaraghavulu, S. Buddhudu, G. Bhaskar Kumar, *Ceram. Int.* **2011**, *37*, 1245.
 [40] H. L. Ma, J. Y. Yang, Y. Dai, Y. B. Zhang, B. Lu, G. H. Ma, *Appl. Surf. Sci.* **2007**, *253*, 7497.
 [41] M. M. Rahman, J.-Z. Wang, M. F. Hassan, D. Wexler, H. K. Liu, *Adv. Energy Mater.* **2011**, *1*, 212.
 [42] X. Guo, C. Wang, M. Chen, J. Wang, J. Zheng, *J. Power Sources* **2012**, *214*, 107.
 [43] G. N. Zhu, H. J. Liu, J. H. Zhuang, C. X. Wang, Y. G. Wang, Y. Y. Xia, *Energy Environ. Sci.* **2011**, *4*, 4016.
 [44] T. Palomäki, M. A. Caro, N. Wester, S. Sainio, J. Etula, L.-S. Johansson, J. G. Han, J. Koskinen, T. Laurila, *Electroanalysis* **2019**, *31*, 746.
 [45] Y. Wang, A. Zhou, X. Dai, L. Feng, J. Li, J. Li, *J. Power Sources* **2014**, *266*, 114.
 [46] S. Goriparti, E. Miele, F. De Angelis, E. Di Fabrizio, R. Proietti Zaccaria, C. Capiglia, *J. Power Sources* **2014**, *257*, 421.
 [47] J. Bohlmark, J. T. Gudmundsson, J. Alami, M. Lattem, U. Helmersson, *IEEE Trans. Plasma Sci.* **2005**, *33*, 1129.
 [48] J. Bohlmark, U. Helmersson, M. VanZeeland, I. Axnäs, J. Alami, N. Brenning, *Plasma Sources Sci. Technol.* **2004**, *13*, 654.
 [49] N. Martin, A. M. E. Santo, R. Sanjinés, F. Lévy, *Surf. Coat. Technol.* **2001**, *138*, 77.
 [50] N. J. Dudney, J. B. Bates, R. A. Zuhr, C. F. Luck, J. D. Robertson, *Solid State Ionics* **1992**, *53–56*, 655.
 [51] S. Sanzaro, E. Smecca, G. Mannino, C. Bongiorno, G. Pellegrino, F. Neri, G. Malandrino, M. R. Catalano, G. G. Condorelli, R. Iacobellis, L. De Marco, C. Spinella, A. La Magna, A. Alberti, *Sci. Rep.* **2016**, *6*, 39509.
 [52] R. Gunnarsson, I. Pilch, R. D. Boyd, N. Brenning, U. Helmersson, *J. Appl. Phys.* **2016**, *120*, 044308.
 [53] B. Geetha Priyadarshini, S. Aich, M. Chakraborty, *Bull. Mater. Sci.* **2014**, *37*, 1691.
 [54] Y. Bi, T. Wang, M. Liu, R. Du, W. Yang, Z. Liu, Z. Peng, Y. Liu, D. Wang, X. Sun, *RSC Adv.* **2016**, *6*, 19233.
 [55] Q. Xia, N. Jabeen, S. V. Savilov, S. M. Aldoshin, H. Xia, *J. Mater. Chem. A* **2016**, *4*, 17543.
 [56] K. Sun, T. S. Wei, B. Y. Ahn, J. Y. Seo, S. J. Dillon, J. A. Lewis, *Adv. Mater.* **2013**, *25*, 4539.
 [57] S. Bhattacharya, A. R. Riahi, A. T. Alpas, *Carbon* **2014**, *77*, 99.
 [58] M. Laitinen, M. Rossi, J. Julin, T. Sajavaara, *Nucl. Instrum. Methods Phys. Res., Sect. B* **2014**, *337*, 55.
 [59] K. Arstila, J. Julin, M. I. Laitinen, J. Aalto, T. Konu, S. Kärkkäinen, S. Rahkonen, M. Raunio, J. Itkonen, J.-P. Santanen, T. Tuovinen, T. Sajavaara, *Nucl. Instrum. Methods Phys. Res., Sect. B* **2014**, *331*, 34.